

Unsteady supersonic aerodynamics based on BEM, including thickness effects in aeroelastic analysis

N. Soltani^{a,*}, V. Esfahanian^a, H. Haddadpour^b, M. Behbahani-Nejad^c

^a *Mechanical Engineering Department, University of Tehran, North Amir-Abad Avenue, Tehran, Iran*

^b *Department of Aerospace Engineering, Sharif University of Technology, Tehran, Iran*

^c *Department of Mechanical Engineering, Chamran University of Ahwaz, Ahwaz, Iran*

Received 22 November 2001; accepted 16 April 2004

Abstract

A general three-dimensional aeroelastic solver is developed based on coupled finite element and boundary element methods and applied to investigate the flutter boundaries in supersonic flows. The boundary element method is applied to three-dimensional unsteady supersonic potential flow as the aerodynamic model and coupled with the finite element method for structural modelling, in order to construct the system of aeroelastic equations. The aeroelastic equations are solved for the flutter prediction using the frequency domain approach. Flutter boundaries for two types of wing planforms at supersonic speeds are determined and compared with the existing experimental results and previous numerical investigations which show good agreement.

© 2004 Published by Elsevier Ltd.

1. Introduction

Aeroelasticity is concerned with phenomena involving the interaction among inertial, elastic, and aerodynamic forces. One of the famous problems in aeroelasticity is supersonic flutter which is of prime interest to designers of high speed flight vehicles. Using an unsteady Euler or Navier–Stokes computational fluid dynamics (CFD) algorithm coupled with a structural dynamics solver, the complete aeroelastic response can be predicted [Farhat and Lesoinne (1996)]. However, the major limitation of applying such a CFD model is the computational time and memory required to run a full aeroelastic simulation of even a simple three-dimensional geometry. Consequently, aeroelasticians prefer to use simpler aerodynamic models such as piston theory (Ashley and Zartarian 1956), the modified Karman–Moore method (Soltani et al. 2000), and harmonic gradient methods (Liu et al., 1991) for supersonic flutter analysis. Hence, if an accurate and efficient replacement for the CFD solver could be developed, aeroelastic response predictions would be much more efficient computationally.

Jones and Appa (1977) used the potential gradient method to analyze unsteady supersonic flows over wings with control surfaces. Chen and Liu (1983) applied the harmonic gradient method for unsteady supersonic flow calculations and Liu et al. (1991) developed the ZONA 51C code based on the acceleration potential formulation of the harmonic gradient method, in order to facilitate the computation scheme of wing-body combinations. Liu et al. (1997) developed a lifting surface method that generalizes linear theory to include the effects of nonlinear thickness and upstream influence in a unified supersonic–hypersonic flow regime.

*Corresponding author.

E-mail addresses: nsoltani@ut.ac.ir (N. Soltani), haddadpour@sharif.edu (H. Haddadpour).

The purpose of the present work is to develop a suitable aerodynamic model which is capable of estimating the unsteady pressure distribution around a three-dimensional structure at supersonic speeds accurately and efficiently with the ability of coupling with the structural model to produce a practical aeroelastic solver. For such a technique to be of practical use, it must be applicable to any arbitrary three-dimensional structure and be easy to implement.

The boundary element method (BEM) is known as a powerful numerical technique in engineering analysis which is capable of coupling easily with the finite element method (FEM). Initially, this method was used in linear problems, but it developed quickly to analyze nonlinear problems too. One of the main advantages of BEM is reduction of the problem dimensionality by one, since it will be required to discretize just the boundary of the computational domain.

In this context, the direct BEM with higher-order elements is applied to the three-dimensional linearized unsteady supersonic potential flow. One of the problems for supersonic flow analysis using BEM is the question of the diaphragm for subsonic leading edge configurations. It is reported by Morino et al. (1975) that for subsonic leading edge configurations the same results are obtained with or without diaphragms. Another problem in potential flow analysis is wake modelling. However, in supersonic flows over conventional configurations, trailing edges usually are supersonic and the wake has no influence on the body; hence its effect is considered to be zero. Discussion is provided on how we can remove hypersingularity on the line of Mach cone intersection with the element. Moreover, the numerical treatment for computing hypersingular boundary integrals is also studied in detail. The results are compared with existing numerical results and exact solutions. Coupling of BEM and FEM is made using surface spline interpolation resulting in a system of aeroelastic equations.

2. Structural model

The finite element method is used for structural modelling. Linear behavior for the structure is a reasonable assumption for the determination of the flutter boundaries. Therefore, the governing equation of structural dynamics can be written as

$$\mathbf{M}\ddot{\mathbf{U}} + \mathbf{C}\dot{\mathbf{U}} + \mathbf{K}\mathbf{U} = \mathbf{F}, \quad (1)$$

where \mathbf{U} , \mathbf{M} , \mathbf{C} , \mathbf{K} , and \mathbf{F} are the vector of structural deflection, mass matrix, damping matrix, stiffness matrix, and nodal forces vector, respectively.

3. Aerodynamic model

The isentropic inviscid flow of a perfect gas can be described by the total velocity potential, Φ_T . Furthermore, it is convenient to introduce the perturbation potential ϕ such that

$$\Phi_T = Ux + \phi, \quad (2)$$

where U is the freestream velocity. Now, consider the linearized unsteady potential flow that is governed by the following partial differential equation:

$$\nabla^2 \phi - \frac{1}{a_\infty^2} \left(\frac{\partial}{\partial t} + U \frac{\partial}{\partial x} \right)^2 \phi = 0, \quad (3)$$

where a_∞ is the freestream speed of sound. The equivalent boundary integral relation for the above partial differential equation in supersonic flows without wake effect is [Morino (1985)]

$$\begin{aligned} 4\pi E(\vec{X}_*)\Phi(\vec{X}_*, T_*) = & - \oint_{\Sigma} ([\Psi']^{\theta^+} + [\Psi']^{\theta^-}) \frac{H}{R'} d\Sigma + \oint_{\Sigma} ([\Phi]^{\theta^+} + [\Phi]^{\theta^-}) \frac{\partial}{\partial N'} \left(\frac{H}{R'} \right) d\Sigma \\ & - \oint_{\Sigma} \left([\dot{\Phi}]^{\theta^+} \frac{\partial \Theta^+}{\partial N'} + [\dot{\Phi}]^{\theta^-} \frac{\partial \Theta^-}{\partial N'} \right) \frac{H}{R'} d\Sigma, \end{aligned} \quad (4)$$

where the asterisk denotes a collocation point, and X , Y , Z , T , and Φ are the Prandtl–Glauert variables, i.e.

$$X = \frac{x}{\beta \ell}, \quad Y = \frac{y}{\ell}, \quad Z = \frac{z}{\ell}, \quad T = \frac{\beta a_\infty t}{\ell}, \quad \Phi = \frac{\phi}{U\ell}$$

and

$$\beta = \sqrt{M^2 - 1}, \quad []^{\theta} = []_{T=T_*-\theta}, \quad N' = (-N_X, N_Y, N_Z), \quad \dot{\Phi} = \frac{\partial \Phi}{\partial T}, \quad \Psi' = \frac{\partial \Phi}{\partial N'};$$

also,

$$R' = \sqrt{(X - X_*)^2 - (Y - Y_*)^2 - (Z - Z_*)^2}, \quad \Theta^\pm = M(X_* - X) \pm R',$$

$$H = \begin{cases} 1, & X_* - X > \sqrt{(Y - Y_*)^2 + (Z - Z_*)^2}, \\ 0, & X_* - X \leq \sqrt{(Y - Y_*)^2 + (Z - Z_*)^2} \end{cases}$$

and Σ is the transformed boundary in XYZ space, N is the unit normal to Σ , $E(\vec{X}_*) = \frac{1}{2}$ on a smooth surface, and M is freestream Mach number.

Since Eq. (4) is linear, the steady and unsteady problems can be studied by setting

$$\phi = \phi_s + \phi_u \tag{5}$$

and separating the two problems, solving them independently and finally, superimposing the results. In aeroelastic analysis the unsteady part is required. Assuming each time-dependent function as

$$f = \tilde{f}e^{st} = \tilde{f}e^{sT} \tag{6}$$

and using Eq. (4) for the unsteady problem, one can obtain

$$4\pi E(\vec{X}_*)\tilde{\Phi}(\vec{X}_*) = - \oint_{\Sigma} \tilde{\Psi}' \frac{H[e^{-(S\Theta^+)} + e^{-(S\Theta^-)}]}{R'} d\Sigma + \oint_{\Sigma} \tilde{\Phi} \frac{\partial}{\partial N'} \left(\frac{H[e^{-(S\Theta^+)} + e^{-(S\Theta^-)}]}{R'} \right) d\Sigma. \tag{7}$$

The boundary integral Eq. (7) is the basic relation for numerical analysis. For this purpose, Eq. (7) is discretized in a standard way in which the boundary integrals are approximated by a summation of integrals over individual boundary elements, i.e.

$$4\pi E(\vec{X}_*)\tilde{\Phi}(\vec{X}_*) = - \sum_{j=1}^m \int_{\Sigma_j} \tilde{\Psi}' \frac{H[e^{-(S\Theta^+)} + e^{-(S\Theta^-)}]}{R'} d\Sigma_j + \sum_{j=1}^m \int_{\Sigma_j} \tilde{\Phi} \frac{\partial}{\partial N'} \left(\frac{H[e^{-(S\Theta^+)} + e^{-(S\Theta^-)}]}{R'} \right) d\Sigma_j. \tag{8}$$

With some mathematical manipulations, it can be shown that Eq. (8) can be expressed as follows:

$$4\pi E(\vec{X}_*)\tilde{\Phi}(\vec{X}_*) = - \sum_{j=1}^m \int_{\Sigma_j} K_1(S, R') \tilde{\Psi}' \frac{H}{R'} d\Sigma_j + \sum_{j=1}^m \int_{\Sigma_j} K_2(S, R') \tilde{\Phi} \frac{\partial}{\partial N'} \left(\frac{H}{R'} \right) d\Sigma_j, \tag{9}$$

where

$$K_1(S, R') = (e^{SR'} + e^{-SR'})e^{SM\Delta X}, \tag{10}$$

$$K_2(S, R') = [e^{SR'} + e^{-SR'} - SR'(e^{SR'} - e^{-SR'})]e^{SM\Delta X}. \tag{11}$$

If one assumes constant K_1 and K_2 over each element, Eq. (9) can be written as

$$4\pi E(\vec{X}_*)\tilde{\Phi}(\vec{X}_*) = - \sum_{j=1}^m K_1(S, R') \int_{\Sigma_j} \tilde{\Psi}' \frac{H}{R'} d\Sigma_j + \sum_{j=1}^m K_2(S, R') \int_{\Sigma_j} \tilde{\Phi} \frac{\partial}{\partial N'} \left(\frac{H}{R'} \right) d\Sigma_j. \tag{12}$$

Using linear elements, two types of surface integrals are produced, i.e.

$$P_{1k} = \int_{\Sigma_j} f_k \frac{H}{R'} d\Sigma_j, \quad k = 1, \dots, 4, \tag{13}$$

$$P_{2k} = \int_{\Sigma_j} f_k \frac{\partial}{\partial N'} \left(\frac{H}{R'} \right) d\Sigma_j, \quad k = 1, \dots, 4. \tag{14}$$

For elements that are intersected by the Mach fore-cone (see Fig. 1), the first integral is weakly singular and the latter is hypersingular at the Mach cone intersection. In Eqs. (13) and (14), f_k are the so-called interpolation functions for bilinear surface elements.

As is shown in Fig. 1, some of the elements are completely inside, completely outside or partially inside the Mach cone. It is obvious that the integrals P_{1k} and P_{2k} are zero when the element Σ_j is completely outside the Mach cone. On the other hand, when Σ_j is completely inside the Mach cone and has no contact with the surface of the Mach cone, P_{1k} and P_{2k} can be evaluated using the Gauss quadrature technique. However, when the element Σ_j is partially inside the Mach cone, the weakly singular integrals P_{1k} can be evaluated using the Gauss quadrature technique with Telles transformation (Telles, 1987) while the integrals P_{2k} have some complexity in their numerical evaluation. For

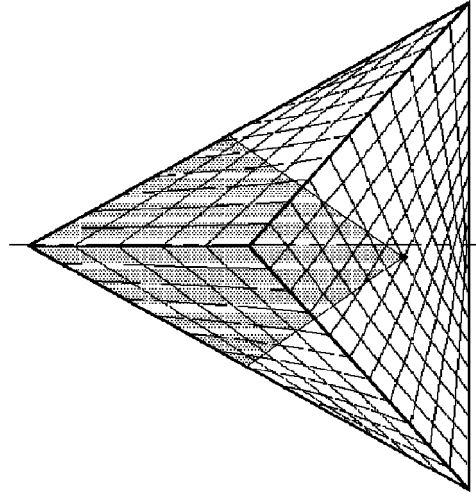


Fig. 1. Mach fore-cone intersection with the boundary elements.

computing the integrals P_{2k} we encounter with four integrals as

$$I_1 = \int_{\Sigma_j} \frac{\partial}{\partial N'} \left(\frac{H}{R'} \right) d\Sigma_j, \quad I_2 = \int_{\Sigma_j} \xi_1 \frac{\partial}{\partial N'} \left(\frac{H}{R'} \right) d\Sigma_j, \tag{15}$$

$$I_3 = \int_{\Sigma_j} \xi_2 \frac{\partial}{\partial N'} \left(\frac{H}{R'} \right) d\Sigma_j, \quad I_4 = \int_{\Sigma_j} \xi_1 \xi_2 \frac{\partial}{\partial N'} \left(\frac{H}{R'} \right) d\Sigma_j. \tag{16}$$

For evaluation of the integrals I_k , at first, the inside part of the element is mapped to a rectangular region with the local coordinates η_1 and η_2 . Therefore, we deal with the following integrals:

$$\begin{aligned} J_1 &= \int_{-1}^1 \int_{-1}^1 \frac{\vec{R} \cdot \vec{a}_1 \times \vec{a}_2}{R^3} d\eta_1 d\eta_2, & J_2 &= \int_{-1}^1 \int_{-1}^1 \eta_1 \frac{\vec{R} \cdot \vec{a}_1 \times \vec{a}_2}{R^3} d\eta_1 d\eta_2, \\ J_3 &= \int_{-1}^1 \int_{-1}^1 \eta_2 \frac{\vec{R} \cdot \vec{a}_1 \times \vec{a}_2}{R^3} d\eta_1 d\eta_2, & J_4 &= \int_{-1}^1 \int_{-1}^1 \eta_1 \eta_2 \frac{\vec{R} \cdot \vec{a}_1 \times \vec{a}_2}{R^3} d\eta_1 d\eta_2, \\ J_5 &= \int_{-1}^1 \int_{-1}^1 \eta_1 \eta_2^2 \frac{\vec{R} \cdot \vec{a}_1 \times \vec{a}_2}{R^3} d\eta_1 d\eta_2, & J_6 &= \int_{-1}^1 \int_{-1}^1 \eta_1^2 \eta_2 \frac{\vec{R} \cdot \vec{a}_1 \times \vec{a}_2}{R^3} d\eta_1 d\eta_2, \\ J_7 &= \int_{-1}^1 \int_{-1}^1 \eta_1^2 \frac{\vec{R} \cdot \vec{a}_1 \times \vec{a}_2}{R^3} d\eta_1 d\eta_2, & J_8 &= \int_{-1}^1 \int_{-1}^1 \eta_2^2 \frac{\vec{R} \cdot \vec{a}_1 \times \vec{a}_2}{R^3} d\eta_1 d\eta_2, \end{aligned}$$

where \vec{a}_1 and \vec{a}_2 are tangent vectors in η_1 and η_2 directions, respectively. Using the Hadamard finite part, one obtains the following relation for the integral J_1 [Morino (1974)]:

$$J_1 = I_D(+1, +1) - I_D(+1, -1) - I_D(-1, +1) + I_D(-1, -1), \tag{17}$$

where

$$I_D(\eta_1, \eta_2) = \tan_p^{-1} \left(\frac{-\vec{R} \times \vec{a}_1 \odot \vec{R} \times \vec{a}_2}{R'(\vec{R} \cdot \vec{a}_1 \times \vec{a}_2)} \right), \quad -\frac{\pi}{2} \leq \tan_p^{-1}(\cdot) \leq \frac{\pi}{2}$$

and

$$\vec{a} \odot \vec{b} = a_x b_x - a_y b_y - a_z b_z$$

is the supersonic dot product.

With some mathematical manipulation, one has

$$\begin{aligned}
 J_1 &= A - B - C + D, \\
 J_2 &= A - B + C - D + F - E, \\
 J_3 &= A + B - C - D + H - G, \\
 J_4 &= A + B + C + D - E - F - G - H + M, \\
 J_5 &= A - B + C - D - E + F - 2K - 2L + 2O, \\
 J_6 &= A + B - C - D - G + H - 2I - 2J + 2N, \\
 J_7 &= A - B - C + D - 2I + 2J, \\
 J_8 &= A - B - C + D - 2K + 2L,
 \end{aligned}$$

where

$$\begin{aligned}
 A &= I_D(+1, +1), & B &= I_D(+1, -1), \\
 C &= I_D(-1, +1), & D &= I_D(-1, -1), \\
 E &= \int_{-1}^1 I_D(\eta_1, +1) d\eta_1, & F &= \int_{-1}^1 I_D(\eta_1, -1) d\eta_1, \\
 G &= \int_{-1}^1 I_D(+1, \eta_2) d\eta_2, & H &= \int_{-1}^1 I_D(-1, \eta_2) d\eta_2, \\
 I &= \int_{-1}^1 \eta_1 I_D(\eta_1, +1) d\eta_1, & J &= \int_{-1}^1 \eta_1 I_D(\eta_1, -1) d\eta_1, \\
 K &= \int_{-1}^1 \eta_2 I_D(+1, \eta_2) d\eta_2, & L &= \int_{-1}^1 I_D(-1, \eta_2) d\eta_2, \\
 M &= \int_{-1}^1 \int_{-1}^1 I_D(\eta_1, \eta_2) d\eta_1 d\eta_2, & N &= \int_{-1}^1 \int_{-1}^1 \eta_1 I_D(\eta_1, \eta_2) d\eta_1 d\eta_2, \\
 O &= \int_{-1}^1 \int_{-1}^1 \eta_2 I_D(\eta_1, \eta_2) d\eta_1 d\eta_2.
 \end{aligned}$$

Applying Eq. (8) at all of the collocation points, and evaluating surface integrals as explained before, one arrives at a set of algebraic equations that can be written in matrix form as

$$\mathbf{A}\tilde{\Phi} = \mathbf{B}\tilde{\Psi}'. \tag{18}$$

3.1. Error study

To validate the present mappings and analytical relations, an element with the following corners is considered:

$$\mathbf{R}(-1, -1) = \begin{Bmatrix} 2 \\ 0 \\ 0 \end{Bmatrix}, \quad \mathbf{R}(1, -1) = \begin{Bmatrix} 2 \\ 1 \\ 0 \end{Bmatrix}, \quad \mathbf{R}(1, 1) = \begin{Bmatrix} 2 \\ 1 \\ 1 \end{Bmatrix}, \quad \mathbf{R}(-1, 1) = \begin{Bmatrix} 2 \\ 0 \\ 1 \end{Bmatrix}.$$

The surface of element is divided into some regions such that all of the possible forms of intersection of the element by the Mach cone can be generated. When the element is intersected as shown in Fig. 2(a) (Arrangement 1) or Fig. 2(b) (Arrangement 2), the element is divided into regions I and II as shown at the top of Tables 1 and 2. Moreover, when the element is intersected as shown in Fig. 2(c) (Arrangement 3), the element is divided into three regions I, II and III as shown at the top of Table 3. Then the integrals I_1 – I_4 are evaluated separately on each region in consideration, with the corresponding mapping relations. In addition, the integrals I_1 – I_4 are evaluated for the whole surface of the element and the results are considered as exact solutions. Finally, the summation of the solutions on each region must be equal to the corresponding exact solution with an acceptable error.

Results for arrangement 1 are presented in Table 1. Comparison of the results with the exact solutions shows excellent agreement for evaluation of I_1 – I_3 while a small relative error exists in evaluation of I_4 . Although this error is very small and acceptable, it arises from more multiple numerical integrations in the corresponding relation and also the higher sensitivity of I_4 because of its smaller order value relative to the I_1 – I_3 . However, this error exists for one element and when the effects of all of the elements inside the Mach cone are computed, the overall error will be very smaller.

Table 2 shows the results of evaluations of I_1 – I_4 for Arrangement 2. The value of ϵ which is shown in Fig. 2(b), is set equal to the one percent of d which is shown in Fig. 2(b). However, with this approximation the values of I_1 – I_4 are in

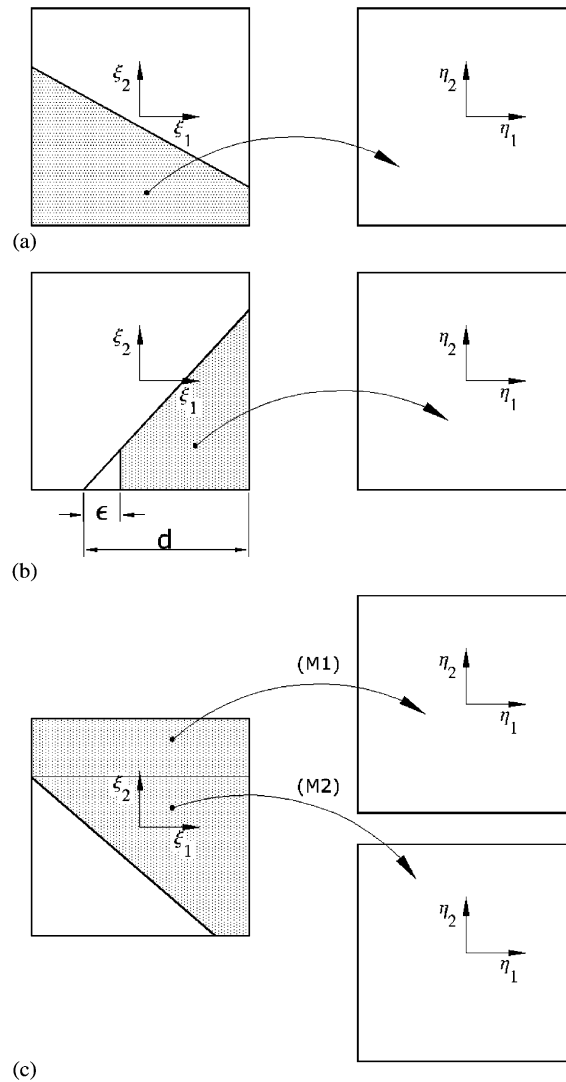


Fig. 2. Corresponding mappings for each arrangement (a) Arrangement 1; (b) Arrangement 2; (c) Arrangement 3.

excellent agreement with the exact solutions, although the relative error in evaluation of I_4 is again greater than the others. Also, the results for evaluation of I_1 – I_4 are presented in Table 3 for Arrangement 3. Similarly, the maximum error is occurred for evaluation of I_4 and has the same order as for the other arrangements.

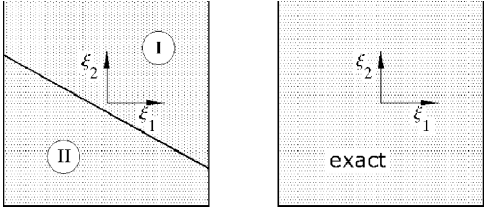
3.2. Aerodynamic loads

The right-hand side of structural operator is the aerodynamic load vector. The aerodynamic load vector is derived from the pressure distribution at the aerodynamic grid points. When the perturbation potential is computed, the pressure distribution can be evaluated using unsteady linearized Bernoulli's theorem as

$$p = -\rho \left(\frac{\partial \phi_u}{\partial t} + U \frac{\partial \phi_u}{\partial x} \right). \quad (19)$$

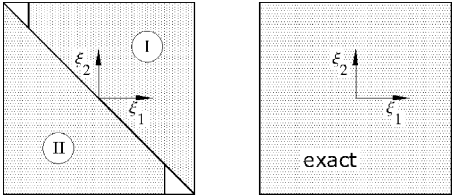
The three-dimensional (3-D) linearized potential flow theory is used to predict the aerodynamic loading and is valid for very thin sections. On the other hand, thickness effects has nonlinear behavior and could render a forward shift in the aerodynamic center for the wings, thereby reducing the flutter speed [Liu et al. (1997)]. This effect will become

Table 1
Present results for Arrangement 1



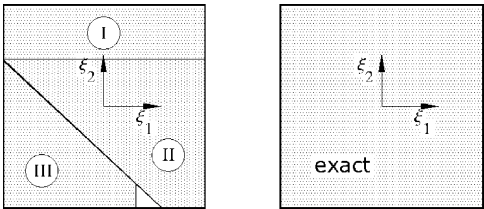
Parameter	Region I	Region II	Region I + II	Exact	Error (%)
I_1	1.9607e-1	1.4376e-1	3.3984e-1	3.3984e-1	0.00
I_2	3.0673e-2	-5.8328e-2	-2.7655e-2	-2.7655e-2	0.00
I_3	5.7799e-2	-8.5463e-2	-2.7664e-2	-2.7655e-2	0.03
I_4	-4.3045e-3	8.0583e-3	3.7539e-3	3.8890e-3	3.47

Table 2
Present results for Arrangement 2



Parameter	Region I	Region II	Region I + II	Exact	Error (%)
I_1	1.4333e-1	1.9647e-1	3.3980e-1	3.3984e-1	0.01
I_2	4.5032e-2	-7.2687e-2	-2.7655e-2	-2.7655e-2	0.00
I_3	4.5224e-2	-7.2889e-2	-2.7665e-2	-2.7655e-2	0.04
I_4	-4.0853e-3	7.8444e-3	3.7591e-3	3.8890e-3	3.34

Table 3
Present results for Arrangement 3



Parameter	Region I	Region II	Region III	Region I + II + III	Exact	Error (%)
I_1	3.6163e-2	1.4660e-1	1.5706e-1	3.3982e-1	3.3984e-1	0.01
I_2	-2.5969e-3	4.5409e-2	-7.0276e-2	-2.7463e-2	-2.7655e-2	0.69
I_3	3.1638e-2	1.0970e-2	-7.0462e-2	-2.7855e-2	-2.7655e-2	0.72
I_4	-2.2717e-3	-1.3857e-2	1.9879e-2	3.7508e-3	3.8890e-3	3.55

increasingly important as the Mach number increases, and frequency decreases. The thickness effect can be taken into consideration by using the nonlinear potential flow formulation. Although this effect is formally second order, by using the perturbation methods the linear model can be modified approximately, to take the effect of thickness into account.

In this paper, this correction is derived by using the well known generalized expression for the pressure coefficients, i.e.,

$$C_p = \frac{2}{\beta} \left[1 + \frac{M^4(\gamma + 1) - 4\beta^2}{2\beta^3} \frac{dz_t}{dx} + \dots \right] \frac{w_a}{U}. \quad (20)$$

(Van Dyke 1953), where γ is the specific heats ratio and z_t is the local thickness. Retaining the first-order term (linear model), the linearized pressure coefficient will be

$$C_{p_l} = \frac{2}{\beta} \frac{w_a}{U}. \quad (21)$$

Using Eqs. (20) and (21), the pressure coefficient in presence of higher-order thickness effects, may be written as

$$C_p = \left[1 + \frac{M^4(\gamma + 1) - 4\beta^2}{2\beta^3} \frac{dz_t}{dx} + \dots \right] C_{p_l}. \quad (22)$$

In the present study, the above 2-D formulation is applied for 3-D problems, where C_{p_l} is computed using a 3-D linearized unsteady potential solver. Therefore, the pressure distribution can be expressed as

$$p = -\rho \left(\frac{\partial \phi_u}{\partial t} + U \frac{\partial \phi_u}{\partial x} \right) \left[1 + \frac{M^4(\gamma + 1) - 4\beta^2}{2\beta^3} \frac{dz_t}{dx} + \dots \right], \quad (23)$$

where the expression in the bracket is the thickness correction factor. For delta or swept wings, the thickness correction factor is evaluated using the normal Mach number. By using the potential function distribution in each element, in terms of the shape functions and nodal values, i.e.,

$$\phi_u = \mathbf{N} \phi_{el}, \quad (24)$$

the pressure distribution is determined as

$$p = -\rho \left(\mathbf{N} \frac{\partial \phi_{el}}{\partial t} + U \frac{\partial \mathbf{N}}{\partial x} \phi_{el} \right) \left[1 + \frac{M^4(\gamma + 1) - 4\beta^2}{2\beta^3} \frac{dz_t}{dx} + \dots \right]. \quad (25)$$

Finally, the pressure distribution can be transferred to the nodal normal force vector by the following well-known relation:

$$\mathbf{F}_{a_{el}}^n = \int_{s_{el}} \mathbf{N}^T p \, ds_{el}, \quad (26)$$

which leads to

$$\mathbf{F}_{a_{el}}^n = -\rho \left(\mathbf{C}_{el} \frac{\partial \phi_{el}}{\partial t} + U \mathbf{D}_{el} \phi_{el} \right). \quad (27)$$

When Eq. (27) is assembled for all the aerodynamic elements, one has

$$\mathbf{F}_a^n = -\rho \left(\mathbf{C} \frac{\partial \phi}{\partial t} + U \mathbf{D} \phi \right). \quad (28)$$

The above relation is used for evaluating aerodynamic loads on each aerodynamic grid point.

3.3. Interpolation

Since usually the aerodynamic and structural meshes do not coincide (see Fig. 3), one needs a suitable surface interpolation. Using surface spline interpolation, one obtains an interpolation matrix, \mathbf{G} , which relates the structural grid point deflection components, \mathbf{U}_s , (including displacements and rotations) to the aerodynamic grid point components, \mathbf{U}_a , by the following relation (Harder and Desmarais 1972):

$$\mathbf{U}_a = \mathbf{G} \mathbf{U}_s. \quad (29)$$

The next step is to find a transformation between the aerodynamic and structural force system. Equivalent virtual work for the two systems of forces (including axial forces and moments) are applied and the result can be written as

$$\mathbf{F}_s = \mathbf{G}^T \mathbf{F}_a. \quad (30)$$

Eqs. (29)–(30) are used to interconnect the noncoincident aerodynamic and structural grid points for the aeroelastic formulation.

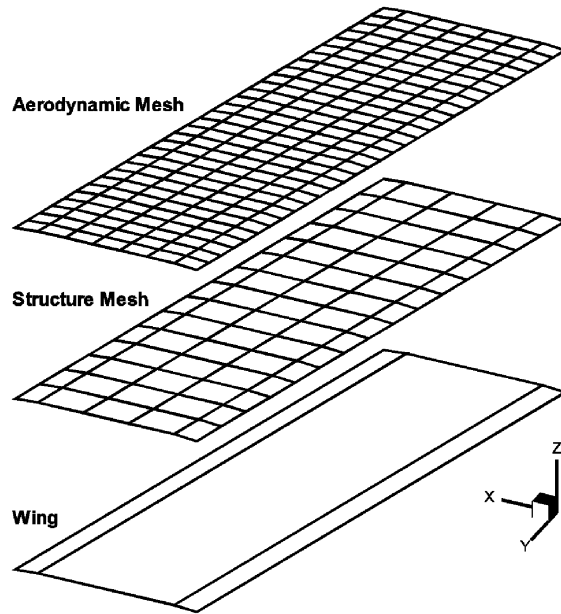


Fig. 3. FEM and BEM mesh on 15° untapered swept wing.

3.4. Downwash

Assuming harmonic motion and neglecting higher order terms the boundary conditions yield [Morino (1974)]

$$\tilde{\Psi}' = -N_Z \left(\frac{\beta}{M} S \tilde{Z} + \frac{1}{\beta} \frac{\partial \tilde{Z}}{\partial X} \right) = -\frac{\tilde{w}_a}{U}. \tag{31}$$

The aerodynamic downwash can be written in terms of structural displacement according to Eq. (29) as

$$\tilde{\Psi}' = -\frac{1}{U} (s\Gamma + UL) \tilde{U}_s, \tag{32}$$

where Γ and L are submatrices of G .

4. Aeroelastic model

Aerodynamic and structural models along with interpolation matrices, aerodynamic loads, and downwashes can be combined to give the aeroelastic model. Using Eqs. (1), (18), (28), and (32), with some manipulations, one arrives at the system of nondimensional aeroelastic equations as

$$\left[k^2 \mathbf{M} + \frac{l^2}{U^2} \mathbf{K} + \mathbf{Q}(k) \right] \tilde{U}_s = \mathbf{0}, \tag{33}$$

where $\mathbf{Q}(k)$ is the aerodynamic stiffness matrix and the complex reduced frequency is defined as

$$k = \frac{ls}{U}. \tag{34}$$

This formulation is based on structural variables. For flutter analysis purposes, Eq. (33) must be solved for the eigenvalue k . Eq. (33) has a different character depending on the unsteady or quasi-steady aerodynamic formulation. Using unsteady aerodynamics leads to a nonlinear eigenvalue problem while for quasi-steady aerodynamics, it reduces to a standard general matrix eigenvalue problem.

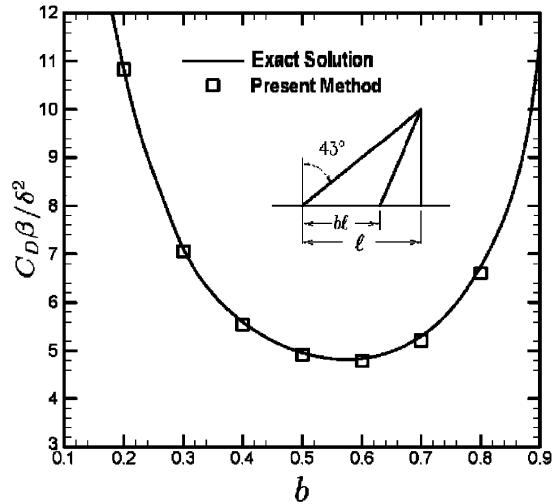


Fig. 4. Thickness drag of a double-wedge delta wing with $M = \sqrt{2}$.

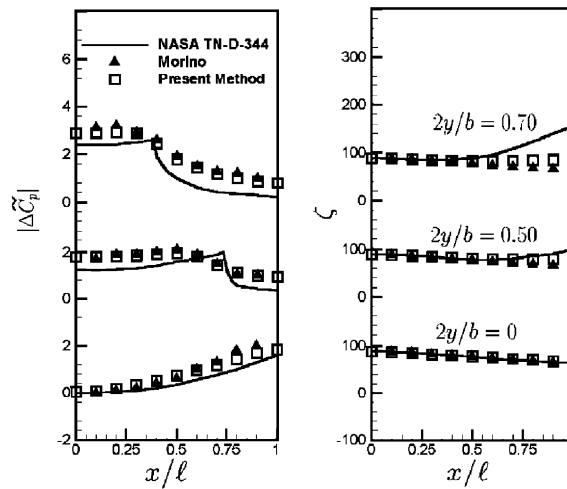


Fig. 5. Absolute value $|\Delta\hat{C}_p|$ and phase angle ζ for rectangular wing oscillating in bending mode with $k = \omega\ell/U_\infty = 0.2$.

5. Numerical results

5.1. Aerodynamic results

The BEM formulation for the aerodynamic model is validated using existing exact solutions (conical flow) in steady state cases (Pukett and Stewart 1947). Fig. 4 shows wave drag due to the thickness for double-wedge delta wing with 45° sweep angle. The surface of the wing is discretized using 250 linear elements. The results show the excellent agreement between the BEM and the exact solution. Results for oscillatory flow are presented in Fig. 5 for a rectangular wing, oscillating in a bending mode

$$z = 0.18043 \left| \frac{2y}{b} \right| + 1.70255 \left| \frac{2y}{b} \right|^2 - 1.13688 \left| \frac{2y}{b} \right|^3 + 0.25387 \left| \frac{2y}{b} \right|^4, \tag{35}$$

with $\omega\ell/U_\infty = 0.2$ and $M = 1.3$. Fig. 5 also shows the results obtained by Morino et al. (1975) and the theory presented by Lessing et al. (1960). The number of elements for the BEM analysis is 10 in both the chordwise and spanwise

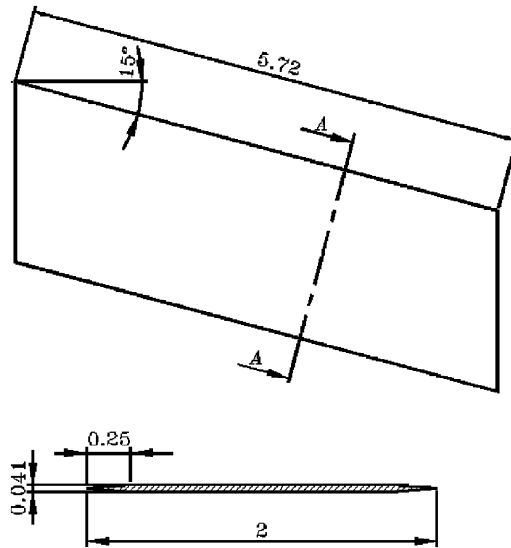


Fig. 6. Fifteen degrees untapered swept wing (all dimensions in inch).

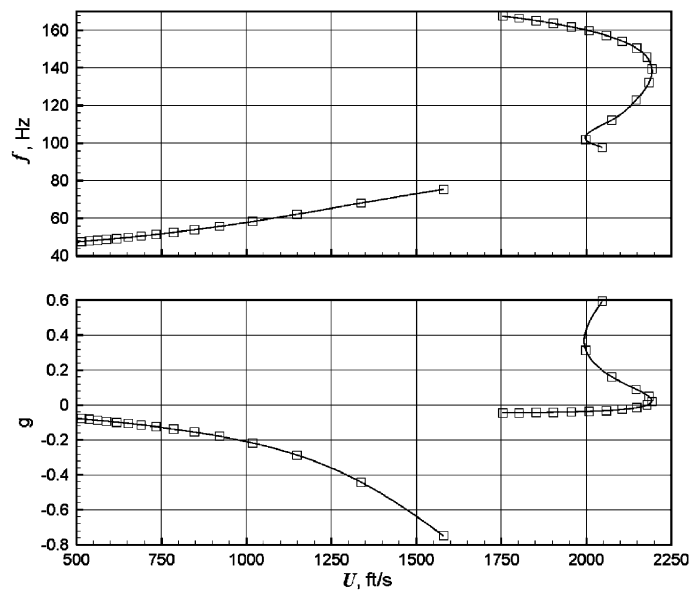


Fig. 7. *K* method results for 45° delta wing at $M = 3$.

directions. The comparison shows good agreement, although for oscillatory flows the evaluation of the coefficients is not as accurate as for steady flows.

5.2. Wing flutter results

Flutter experimental studies were made at NASA Langley Research Center by Tuovila and McCarty (1955). Two types of wings which were cut from sheet metal are selected for performing flutter analysis using the present formulation. The 15° untapered swept wing model of aspect $AR = 5.35$ had the leading and trailing edge beveled $\frac{1}{4}$ -in to form a hexagonal section shape and 2-in chord measured perpendicular to the leading edge with 0.041-in thickness (Fig. 6). The 45° delta wing model leading edge beveled $\frac{1}{8}$ -in with 0.034-in thickness and 6-in chord at root.

Table 4
Flutter boundaries for 45° delta magnesium wing

	$M = 1.3$		$M = 3$	
	$\rho = 0.00066 \text{ slug/ft}^3$		$\rho = 0.00072 \text{ slug/ft}^3$	
	V_f (ft/s)	f_f (Hz)	V_f (ft/s)	f_f (Hz)
Experiment (Tuovila and McCarty, 1955)	1280	150	2030	159
Present work	1163	159	2178	146
Piston theory (without thickness effect)	1427	155	—	—
Piston theory (with thickness effect)	1179	166	—	—

Table 5
Flutter boundaries for 15° swept wing

	$M = 1.3$		$M = 3$	
	Aluminum wing		Magnesium wing	
	$\rho = 0.00049 \text{ slug/ft}^3$		$\rho = 0.00093 \text{ slug/ft}^3$	
	V_f (ft/s)	f_f (Hz)	V_f (ft/s)	f_f (Hz)
Experiment (Tuovila and McCarty, 1955)	1280	102	2030	146
Rodden et al. (1962)	1397	124	1913	149
Rodden (1991)	1547	127	2170	148
Liu et al. (1997)	1397	119	1805	147
Present work	1418	135	1863	145

The results of computed flutter points of the wings at $M = 1.3$ and 3 are presented in Tables 4 and 5, using the K method (Rodden and Johnson 1994); see Fig. 7. The results in Table 4 show the destabilizing effect of the wing thickness which is referred by other investigators.

The results show the flutter parameters obtained by the present method are in good agreement with other investigators and the experiment. However, some discrepancies are seen between the results and the experimental values. The differences are due to the structural modelling of the wings. Natural frequencies of the wings used in the experiment could change slightly due to the different set-up in the experiment. It should be noted that in the present study the structural model weight and second natural frequency are set to the experimental values. Actually, the problem is very sensitive to the boundary conditions and to the structural parameters, which could be the source of discrepancies between the numerical and experimental results.

6. Conclusions

The combination of BEM and FEM is used to develop an accurate, efficient and general aeroelastic tool for three-dimensional supersonic flutter analysis. Direct BEM with higher-order elements is applied to three-dimensional linearized unsteady supersonic potential flow and FEM to the structure. Coupling of BEM and FEM is made using surface spline interpolation and the system of aeroelastic equations are solved in the frequency domain. Flutter boundaries for two types of wing planforms at supersonic speeds are determined and compared with the available experimental and numerical results. Good agreement is obtained, and the results show that the present method is a practical tool for the study of aeroelastic problems and the prediction of aeroelastic instability.

Acknowledgement

The research reported in this paper was supported by the University of Tehran (Grant no. 618-3-857), Which is gratefully acknowledged.

References

- Ashley, H., Zartarian, G., 1956. Piston theory a new aerodynamic tool for the aeroelastician. *Journal of the Aeronautical Sciences* 20, 1109–1118.
- Chen, P.C., Liu, D.D., 1983. A harmonic gradient method for unsteady supersonic flow calculations. AIAA Paper 83-0887.
- Farhat, C., Lesoinne, M., 1996. On the accuracy, stability and performance of the solution of three-dimensional nonlinear transient aeroelastic problems by partitioned procedures. AIAA Paper 96-1388.
- Harder, R.L., Desmarais, R.N., 1972. Interpolation using surface splines. *Journal of Aircraft* 9, 189–191.
- Jones, W.P., Appa, K.A., 1977. Unsteady supersonic aerodynamic theory by the method of potential gradient. *AIAA Journal* 15, 59–65.
- Lessing, H.C., Troutman, J.C., Menees, G.P., 1960. Experimental determination of the pressure distribution on a rectangular wing oscillating in the first bending mode for Mach numbers from 0.24 to 1.30. NASA TN-D-344.
- Liu, D.D., James, D.K., Chen, P.C., Pototzky, A.S., 1991. Further studies of harmonic gradient method for supersonic aeroelastic applications. *Journal of Aircraft* 28, 598–605.
- Liu, D.D., Yao, Z.X., Sarhaddi, D., Chaves, F., 1997. From piston theory to a unified hypersonic supersonic lifting surface method. *Journal of Aircraft* 34, 304–312.
- Morino, L., 1974. A finite element formulation for supersonic flows around complex configurations. TR-74-01, Department of Aerospace Engineering, Boston University.
- Morino, L., 1985. Mathematical foundations of integral equation methods. In: Morino, L. (Ed.), *Computational Methods in Potential Aerodynamics*. Computational Mechanics Publications, Springer, Berlin.
- Morino, L., Chen, L.T., Suci, E.O., 1975. Steady and oscillatory subsonic and supersonic aerodynamics around complex configurations. *AIAA Journal* 13, 368–374.
- Pukkett, A.E., Stewart, H.J., 1947. Aerodynamic performance of delta wings at supersonic speeds. *Journal of Aeronautical Sciences* 14, 567–578.
- Rodden, W.P., 1991. Correction factors for supersonic thickness effects. MSC/NASTRAN-WPR-3, The MacNeal-Schwendler Corporation.
- Rodden, W.P., Johnson, E.H., 1994. MSC/NASTRAN Aeroelastic Analysis Users Guide. The MacNeal-Schwendler Corporation.
- Rodden, W.P., Farkas, E.F., Malcom, H.A., Kliszewski, A.M., 1962. Aerodynamic influence coefficients from piston theory: analytical development and computational procedure. Aerospace Corporation TDR-169 (3230-11) TN-2.
- Soltani, N., Esfahanian, V., Haddadpour, H., 2000. Coupled formulation of structure and aerodynamic with application in panel flutter using eigenanalysis. *Proceedings of Eighth Annual Conference of the CFD Society of Canada*, Vol. 2, Montreal, pp. 737–744.
- Telles, J.C.F., 1987. Self-adaptive coordinate transformation for efficient numerical evaluation of general boundary element integrals. *International Journal of Numerical Methods Engineering* 24, 959–973.
- Tuovila, W.J., McCarty, J.L., 1955. Experimental flutter results for cantilever wing models at Mach numbers up to 3.0. NACA RM L55E11.
- Van Dyke, M.D., 1953. Supersonic flow past airfoils including nonlinear thickness effect. NACA 1183.